



# Synthesis and characterization of solid-state Fe-exchanged nano-bentonite and evaluation of methyl orange adsorption

Nahid Hajipour<sup>1</sup> · Mohammad Ghorbanpour<sup>1</sup> · Majid Safajou-jahankhanemlou<sup>1</sup>

Received: 10 August 2021 / Accepted: 17 February 2022 / Published online: 27 February 2022  
© The Author(s), under exclusive licence to Springer-Verlag GmbH Germany, part of Springer Nature 2022

## Abstract

A new adsorbent was synthesized using ion-exchange between iron salts and bentonite modified with acetyl trimethylammonium bromide (CTAB) in the solid phase. Ion-exchange was performed in the solid state at a temperature of 100 °C for 2 min. Various analyses such as X-ray diffraction (XRD), scanning electron microscopy (SEM), porosity measurement (BET), infrared Fourier transform (FT-IR), transmission electron microscopy (TEM), X-ray energy diffraction (EDX), and thermal weighing (TGA) were used to characterize the synthesized nano-adsorbents. Under optimal conditions (pH = 7, time 60 min, concentration of dye solution 150 ppm, and amount of nano-adsorbent 0.75 g/l), the modified nano-adsorbent absorbed 73% of the methyl orange (MO) dye. Adsorption isotherm studies and kinetic model showed that the pseudo-second-order model and Langmuir equation agree with the obtained results. After three reductions of the modified nano-adsorbent in the photo-Fenton process, the dye absorption percentage was 69.50%.

**Keywords** Solid-state ion exchange adsorption · Surfactant · Modified bentonite with iron · Photo-Fenton

## Introduction

Environmental pollution is one of the global problems that affect biodiversity, ecosystems, and human health. One of the most challenging groundwater contamination problems is paint. Despite limited water resources, the treatment of industrial dye effluents is essential. Dye effluents reduce the penetration of sunlight into the water due to the formation of a visible layer above the water surface and affect photosynthesis, which is a threat to aquatic life (Chacko and Subramaniam 2011). Their contact with the skin irritates and causes shortness of breath when inhaled (Nguyen and Juang 2013). Methyl orange (MO) is one of the most common water-soluble azo dyes widely used in various industries, including textile, cosmetics, paper, printing, and food industries (Zayed et al. 2018). Its effluents are mostly discharged in industrial wastewater. The acute toxicity of MO

dyes is caused by oral ingestion and inhalation, and it is carcinogenic (Lellis et al. 2019). As MO dye is not easily decomposed and resistant to light and washing, it is essential to separate it from the effluent (Yu and Luo 2014; Ghaedi and Mosallanejad 2014). Dye effluents can be treated by biological, chemical, and physical methods (Tang et al. 2018). Nanofiltration, ultrafiltration, membrane filtration, reverse osmosis, and adsorption are among the physical methods of dye effluents treatments. Among the mentioned techniques, adsorption has been widely considered by researchers due to its simplicity and availability (Gong et al. 2011; Agarwal and Singh 2017). Adsorption is a process for separation without the need for special equipment and high electrical energy. This mass transfer process from the effluents to the solid adsorbent is easy to design and does not produce hazardous by-products (Yagub et al. 2014; Rafatullah et al. 2010; Bouabidi et al. 2018). Another feature of the adsorption process is the possibility of regenerating the adsorbent. Today, by identifying low-cost adsorbents, this method is an economical way to remove dye effluents (Ahmad et al. 2015; Mojsov et al. 2016). Adsorption capacity and surface area are the most critical characteristics of adsorbents. Bentonite is an aluminum phyllosilicate clay consisting of montmorillonite (and a small amount of beidellite depending on the sources). Bentonite structure consists octagonal aluminum

---

Responsible Editor: Sami Rtimi

✉ Majid Safajou-jahankhanemlou  
m.safajou@uma.ac.ir

<sup>1</sup> Department of Chemical Engineering, University of Mohaghegh Ardabili, P. O. Box, 56199-11367 Ardabil, Iran

layer sandwiched between two quadrilateral silica layers, which give a high aspect ratio to it (Alexandre et al. 2009; Ballav et al. 2018). Bentonite can be used in a wide range of applications due to its high porosity, high viscosity, and high ion-exchange capacity (Ahmaruzzaman 2008; Doulia et al. 2009). One of the advances in nanomaterials is the use of nano-adsorbents to remove industrial effluents. They are more efficient than traditional adsorbents (Liu et al. 2008; Singh et al. 2011; Simelane et al. 2016; Fosso-Kankeu et al. 2016). To increase the adsorption capacity of bentonite, thermal activation (Al-Asheh et al. 2003), acid activation (Hussin et al. 2011), ion-exchange (Hadjltaief et al. 2014), simultaneous modification with surfactant (Huang et al. 2017), and pillaring (Ma et al. 2005) can be used. The presence of iron oxide nanoparticles on nanolayers makes it possible to regenerate the prepared adsorbent in the photo-Fenton process (Khelifi and Ayari, 2019). In the process of photo-Fenton reduction, organic dyes adsorbed on the adsorbent, in the presence of hydrogen peroxide and ultraviolet light, bind to produced hydroxyl radicals, which leads to the degradation of organic dyes and the production of water, carbon dioxide, and other chemical compounds (Babuponnusami and Muthukumar 2014). In this study, bentonite nanolayers were selected as the adsorbent, and CTAB was used to increase the d-spacing between its layers. The photo-Fenton process was used to regenerate the adsorbent, and acceptable results were obtained. At each stage of surface modification, X-ray diffraction (XRD), energy-dispersive X-ray (EDX), Brunauer–Emmett–Teller (BET) surface area, thermal gravimetric analysis (TGA), and Fourier transform infrared spectroscopy (FTIR) analyses were used to prove success of the modification process. The effect of MO and initial MO concentration, contact time, and adsorbent amount on adsorption performance was investigated. Also, isotherms and adsorption kinetics were studied, and thermodynamic studies were used to investigate the adsorption process.

## Experimental

Bentonite (B, the surface area of 85.03 m<sup>2</sup>/g, basal spacing of 1.40 nm, and moisture content of ≤ 10.00 wt.%) kindly provided by Kanyasazejam Co. Cetyltrimethylammonium bromide (CTAB, ≥ 98%), iron(II) chloride tetrahydrate (FeCl<sub>2</sub>·4H<sub>2</sub>O, ≥ 99%), hydrogen peroxide (H<sub>2</sub>O<sub>2</sub>, 30% w/v), chloridric acid (HCL, 37%), sodium hydroxide (NaOH, ≥ 99%), and methyl orange (MO) were purchased from Merck.

According to procure (Huang et al. 2017; Darvishi and Morsali 2011), the 4 g of bentonite was dispersed in 200 ml deionized water (20 g/L) under vigorous stirring for 72 h. In the next step, 100% cation-exchange capacity of the bentonite, CTAB was added to the mixture.

After ultrasonication with acoustic intensity of 400 W for 30 min at 50 °C, the resulting slurry was washed and centrifuged (at 6000 rpm) three times to remove bromide ion. Then, it was dried at 50 °C for 24 h, and the obtained pretreated bentonite was named B-CTAB. For pillaring, 0.5 g of B-CTAB was sonicated with 1 g of FeCl<sub>2</sub>·4H<sub>2</sub>O in the aqueous phase, then the mixture was centrifuged three times with distilled water to ensure the removal of residual ions, and finally dried at 50 °C overnight. The dried powder was collected and named B-CTAB-Fe. The color of B-CTAB changed from white to cream during the pillaring process.

Transmission electron microscopy was performed by a Phillips EM 208 S 100 kV. The bentonite samples were embedded and then cut with an ultramicrotome into layers with 60–100-nm thickness, which were cryo-ultramicrotome at – 145 °C with a diamond knife cooled at – 60 °C. Morphology of samples was analyzed by a scanning electron microscope (SEM) (LEO model 1430 VP, England) equipped with a backscattered electrons detector. Before analysis, all samples were coated with a thin layer of gold palladium using an Edwards S-150 sputter coater (Wilmington, MA, USA). The elements in the samples were observed using energy-dispersive spectroscopy (EDS) (Mira 3-XMU, Berno, Czech Republic). Sample X-ray diffraction (XRD) patterns were collected on an Intel, France, EQUINOX 3000 X-ray diffraction with Cu K $\alpha$  radiation, while the accelerating voltage and applied currents were 40 kV and 30 mA, respectively. Thermal gravimetric analyses (TGA) of the prepared polymers and composites were performed on a LENSES STAPT-1000 instrument (Linseis STA PT1000, Selb, Germany) using about 4 mg of material as a probe. The samples were heated up to 700 °C with a heating rate of 10 °C·min<sup>-1</sup>. The residue in the N<sub>2</sub> atmosphere at 700 °C considers the inorganic content of samples. The FT-IR spectrum of the samples was recorded in the region 4000–400 cm<sup>-1</sup> using a spectrum 400 instrument (PerkinElmer Inc., USA). The Brunauer–Emmett–Teller (BET) surface area measurements of bentonite samples were performed on BELSORP-mini, Bell Japan, Inc. To compare the percentage of methyl orange dye removal and the adsorption capacity of the samples, different amounts of adsorbents (B, B-CTAB, or B-CTAB-Fe) were added to 40 ml of different MO concentrations (20, 75, 100, 125, 150, 175, and 200 ppm) and then placed on a shaker for 2 h. Adsorbent concentration in MO water solution was varied from 0.25 to 4.5 g·L<sup>-1</sup>. To evaluate the effects of the pH, temperature, and time on the absorption process, different pH (ranging from 2 to 9), temperature (303, 313, and 323), and absorption time (from 5 to 120 min) values were used in experiments. After 60 min, the mixture was centrifuged at 60,000 rpm. Dye removal percentage was calculated using Eq. 1.

$$\text{Removal efficiency (\%)} = \left[ \frac{c_0 - c_e}{c_0} \right] \times 100 \quad (1)$$

where  $c_0$  and  $c_e$  denote the MO concentration ( $\text{mg L}^{-1}$ ) at initial and equilibrium time, respectively. Also, the equilibrium capacity ( $q_e$ ) was calculated using Eq. 2.

$$q_e = \frac{c_0 - c_e}{M} \times V \quad (\text{mg/g}) \quad (2)$$

where  $M$  is the weight of adsorbent (g) and  $V$  is the volume of the solution (L).

After adsorption under optimal conditions ( $0.75 \text{ g L}^{-1}$  of B-CTAB-Fe was mixed with 150 ppm of MO at  $\text{pH}=7$  for 60 min), the photo-Fenton process was used to reduce B-CTAB-Fe nano-adsorbent. The B-CTAB-Fe separated by centrifugation at 6000 rpm, then dispersed in 40 ml of distilled water, and the pH of the mixture reached 4. The mixture was introduced into a photoreactor and placed on a magnetic stirrer. The reduction process was performed by adding  $\text{H}_2\text{O}_2$  (22.5 mM) and turning on the UVC lamp (4 W, Philips) for 90 min. The reduced B-CTAB-Fe was separated by centrifugation and dried at  $50^\circ\text{C}$  in an oven for 24 h for reuse.

## Results and discussion

The XRD pattern of B, B-CTAB, and B-CTAB-Fe is shown in Fig. 1. The main peak in the XRD pattern of bentonite appeared at  $36.82^\circ$  and the peak at  $20.08^\circ$ , corresponding to the structural feature of smectites (De León et al. 2017). Also, the peaks at  $2\theta=21.01^\circ$ ,  $26.80^\circ$ , and  $42.73^\circ$  are related to the quartz mineral in bentonite (Khatamian et al. 2019). In this pattern, the peak  $d_{001}$  has changed from  $2\theta=6.28^\circ$  for B to  $2\theta=5.30^\circ$  for B-CTAB. The d-space between the bentonite layers ( $d_{001}$ ) increased from 1.40 nm to 1.66 nm for the surface-modified sample (B-CTAB). Ion-exchange between the surfactant and bentonite has increased the distance between the layers (Dos Santos et al. 2018). The reason for such an increase is the replacement of the long CTAB alkyl chain with cations located between the bentonite layers (Huang et al. 2017). In the B-CTAB-Fe XRD pattern, no characteristic peak related to d-space is observed. The absence of a peak in  $d_{001}$  indicates a very irregularly formed structure called clay exfoliation. So, the layers are delaminated by the polarization, and it seems to be no aggregated layers in its structures (Chen et al. 2017, 1995; Yuan et al. 2006).

SEM images of B, B-CTAB, and B-CTAB-Fe are shown in Fig. 2. Bentonite aggregates have a smooth, irregular surface (Fig. 2a). Bentonite sample after CTAB treatment and sonication forms collapsed structure with more irregularity. Also, in Fig. 2b, bentonite nanosheets are primarily broken.

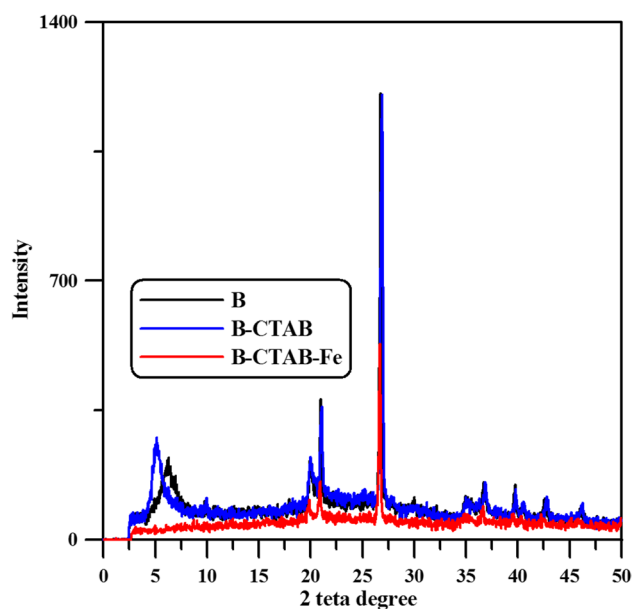


**Fig. 1** XRD spectra in the  $2\theta$  range of  $2.5^\circ$  to  $50^\circ$  for B, B-CTAB, and B-CTAB-Fe

Figure 2c shows the morphology of nanosheets after the iron nanoparticle's entrance. As shown in Fig. 2d TEM image of sample B-CTAB-Fe confirms the entry of iron nanoparticle's into the gallery of clay nanosheets. The TEM image next to the X-ray patterns shows the exfoliation of the clay. Also, the TEM image proves that the synthesis method of B-CTAB-Fe has been successful, and the iron salt has been able to enter the nanometer distance between the clay plates in 2 min at temperature, close to its melting temperature, and the pillaring process has been performed successfully. The darker parts of the images show iron oxide nanoparticles, which are denser and restrict the passage of electrons.

According to the results of Table 1, calcium is present in the interlayer structure of primary bentonite. In the B-CTAB sample, there is 5.41% carbon and no calcium, which indicates that the cation exchange in the B-CTAB sample is complete, and calcium has been removed from the bentonite layers (Dos Santos et al. 2018). Also, removing negative bromide ions indicates proper and sufficient washing and centrifugation. In the B-CTAB-Fe sample, iron ions and the absence of chloride ions indicate the success of iron entry into the bentonite structure and proper washing after the modification process. In the bentonite modification process, iron oxide nanoparticles were exposed to the B-CTAB sample for 2 min. This time is shorter than other studies in the liquid phase (Chen et al. 2017; Hadjiltaief et al. 2014). The low time required in this method for complete removal of calcium and the entry of the surfactant CTAB and the entry of iron oxide nanoparticles into the interlayer space of bentonite indicate the efficiency of this method.

**Fig. 2** SEM images of the Bentonite (a), B-CTAB (b), and BCTAB-Fe (c). TEM image of B-CTAB-Fe (d)

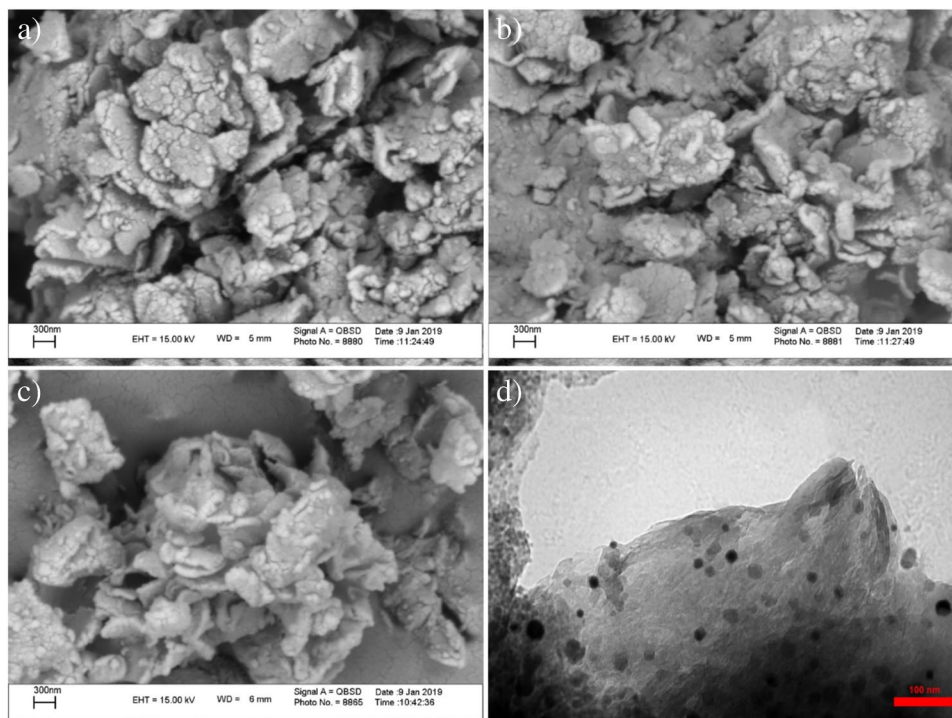


**Table 1** Chemical composition of the Bentonite, B-CTAB, and B-CTAB-Fe

Element	Bentonite	B-CTAB	B-CTAB-Fe
O	55.19	57.15	55.04
Mg	1.58	1.29	1.20
Al	8.10	6.34	6.39
Si	32.80	28.17	29.33
K	0.79	0.97	0.63
Ca	0.61	0	0
Fe	0.92	0.67	2.58
C	0	5.41	4.83

**Table 2** Chemical composition of the bentonite, B-CTAB, and B-CTAB-Fe

Sample	Surface area (m <sup>2</sup> /g)	Pore size (nm)	Pore volume (cm <sup>3</sup> /g)
Bentonite	85.03	1.66	0.11
B-CTAB	35.88	1.66	0.05
B-CTAB-Fe	25.26	1.88	0.04

According to BET results (Table 2), the surface area of bentonite decreased by 49.15 m<sup>2</sup>/g after modification with CTAB. The reduction in surface area and pore volume in the B-CTAB sample is due to the entry of CTAB organic molecules, which leads to the overlap of the nanolayer surface

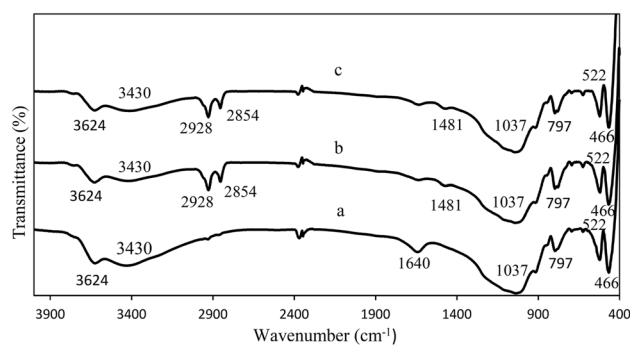


**Fig. 3** FTIR spectra of (a) B, (b) B-CTAB and (c) B-CTAB-Fe

and blocked interlayer channels (Huang et al. 2017). The filling of bentonite pores with large molecules of CTAB and iron seems to have created a small number of larger cavities, in addition to reducing the pore volume. Such a decrease can be attributed to the reduced access of nitrogen molecules to the inner surfaces of nanosheets during the adsorption process (Dos Santos et al. 2018; Deniz and Karaman 2011). In the pillaring process, the specific surface area is reduced by placing oxidized iron nanoparticles in the bentonite structure and closing more cavities.

According to FTIR spectra (Fig. 3), in all samples, the absorption band occurring at 3624 cm<sup>-1</sup> was due to the stretching vibration of the hydroxyl groups of water adsorbed in the bentonite structure (Tyagi et al. 2006). The absorption band at 1640 cm<sup>-1</sup> was the characteristic

of bending vibration of the OH group of water molecules between the bentonite layers (Zhang et al. 2010). The strong absorption band at  $1037\text{ cm}^{-1}$  in the bentonite sample is related to the Si–O stretching vibration. The absorption band at  $797\text{ cm}^{-1}$  is also related to the stretching vibration of Al–O (Li et al. 2016). The absorption peak at  $522\text{ cm}^{-1}$  is related to the layer vibration of the Al–O–Si network (Yan et al. 2016). The absorption peak at  $466\text{ cm}^{-1}$  is attributed to the layer vibration of the Si–O–Si network (Moslemizadeh et al. 2016). Figure 3b shows the FT-IR spectrum of the B-CTAB sample. Absorption occurs at  $2928\text{ cm}^{-1}$  and  $2928\text{ cm}^{-1}$ , subject to symmetric and asymmetric stretching vibrations  $-\text{CH}_2$  and  $-\text{CH}_3$  in the CTAB aliphatic chain (Huang et al. 2017). The presence of a new peak at  $1481\text{ cm}^{-1}$  is related to the flexural vibration of the methyl group (Schampera et al. 2016). FT-IR spectrum of B-CTAB-Fe shows that the heat of the pillaring process did not cause the CTAB degradation. The vibrational absorption peak of the Fe–O band, which should be observed at  $1020\text{ cm}^{-1}$ , is covered by a strong montmorillonite peak (Ma et al. 2005).

The thermal stability of the samples was studied by TGA. Figure 4 shows TGA thermograms for B, B-CTAB, and B-CTAB-Fe samples. The weight loss of bentonite (5.28%) in the temperature range of 40 to  $150\text{ }^\circ\text{C}$  is due to water evaporation absorbed between the bentonite layers (Ma et al. 2005; Gourouza et al. 2011). Mass reduction of bentonite in the temperature range of 550 to  $700\text{ }^\circ\text{C}$  (0.92%) mass is related to bentonite dehydroxylation (Bounab et al. 2017). This high-temperature range causes the crystalline structure of bentonite to fail. The weight reduction of the B-CTAB sample (33%) from ambient temperature to  $150\text{ }^\circ\text{C}$  is due to

the loss of absorbed water on the surface and between the layers (Dos Santos et al. 2018). This amount is lower than unmodified bentonite, because some of the absorbed water in the sample was removed by the CTAB modification process. In the TG graph, from 100 to  $500\text{ }^\circ\text{C}$ , both B-CTAB and B-CTAB-Fe samples have a mass reduction of about 10.16% which is due to the thermal degradation of the surfactant penetrating into the bentonite structure. The organic structure of CTAB decomposes in this temperature range (Ma et al. 2005). The presence of a peak in this temperature range is also a confirmation of the success of bentonite treatment with CTAB. In the temperature range of 500 to  $700\text{ }^\circ\text{C}$ , a mass reduction of 3.52 can be observed, caused by the loss of OH groups in the silicate layers (Ma et al. 2005).

The effect of pH on the adsorption of MO onto B-CTAB-Fe is shown in Fig. 5. The lowest and highest percentages of dye removal were obtained at pH 2 and 7, respectively. At acidic pH, due to the positive surface of the nano-adsorbent and the presence of  $\text{H}^+$  ions, the electrostatic repulsion force between them does not allow dye removal to the nano-adsorbent surface. Because in the competition between  $\text{H}^+$  ions and the positive surface of the nano-adsorbent, the MO (anion dye) is absorbed by  $\text{H}^+$  acid ions. Therefore, with increasing pH and decreasing acidity, dye removal by nano-adsorbent increases. At pH above 7, due to  $\text{OH}^-$  positive ions, the nano-adsorbent surface is covered by these small ions. As a result, the electrostatic repulsion force between the negative MO ions and the negatively absorbed surface charge decreases the dye removal percentage.

The optimum pH value was considered 7 for adsorption experiments. The results showed that with increasing

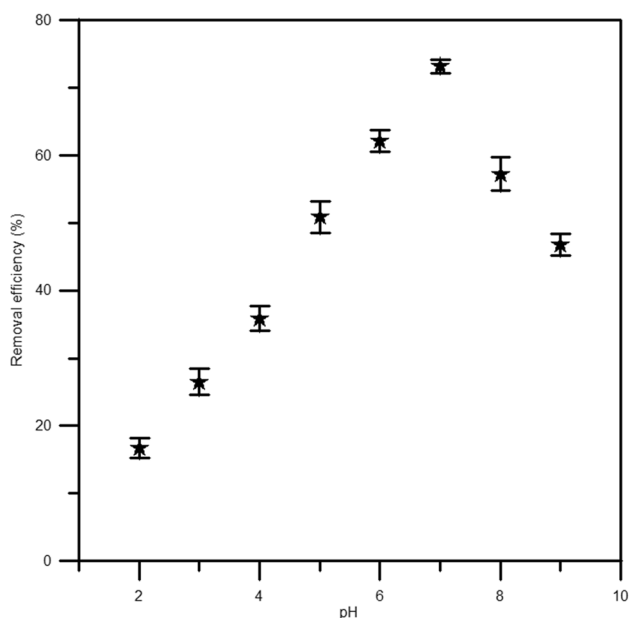


Fig. 4 TGA thermograms for bentonite and modified bentonites

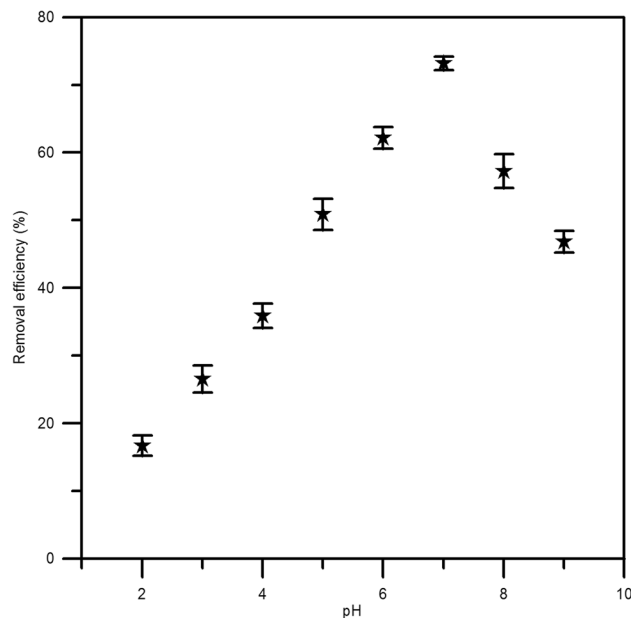


Fig. 5 Effect of pH on the absorption of MO onto B-CTAB-Fe

MO concentration, the equilibrium adsorption capacity has an upward trend (Fig. 6). Above 150 ppm, due to the saturation of adsorption sites on nanosheets, adsorption efficiency decreases.

The effect of contact time on the amount of MO adsorption with a concentration of 150 ppm and a pH of 7 is shown in Fig. 7. The presence of empty adsorption sites on the nano-adsorbent surface in the early times increases the adsorption rate. The time of 60 min can be seen as the equilibrium time of absorption. The percentage of MO removal by bentonite, B-CTAB, and B-CTAB-Fe is 46.8%, 76.88%, and 73.18%, respectively. The B-CTAB-Fe sample is less adsorbed than the B-CTAB sample (approximately 3%) due to the presence of oxidized iron nanoparticles in its structure.

Figure 8 shows the effect of changing the amount of B-CTAB-Fe from 0.25 to 4.5 g/lit at pH = 7, time 60 min, and concentration of 150 ppm. With increasing the amount of nano-adsorbent and increasing the number of active sites, the effluent deposition on the nano-adsorbent surface has increased. The slope of the changes varies from 0.75 g/l onwards. A concentration of 0.75 g/lit is likely to be optimal for the availability of active adsorbent sites.

Absorption isotherms such as Langmuir and Freundlich were used to describe the relationship between the initial concentration of colored effluent and the amount of adsorbed effluent. The linear form of the Langmuir equation (Eq. 3) and Freundlich equation (Eq. 4) is as follows:

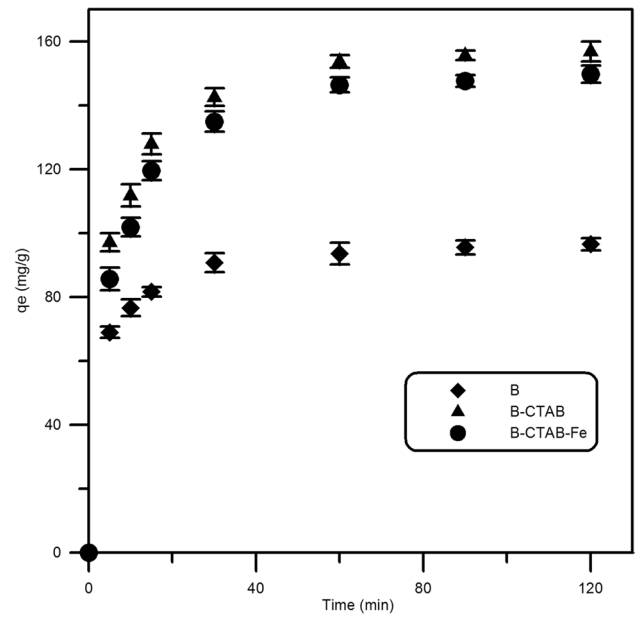


Fig. 7 Effect of contact time on the adsorption of MO onto B, B-CTAB, and B-CTAB-Fe

$$\frac{1}{q_e} = \frac{1}{q_m} + \frac{1}{q_m k_L} \cdot \frac{1}{c_e} \tag{3}$$

$$\log q_e = \log kf + (1/n) \log c_e \tag{4}$$

$q_e$  (mg/g) is the amount of dye adsorbed for a given amount of adsorbent at equilibrium.  $k_L$  (mg/L) is Langmuir

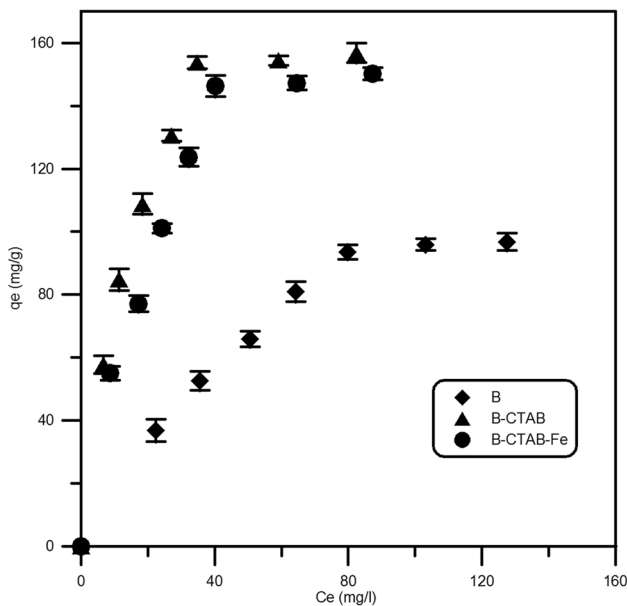


Fig. 6 Effect of initial concentration on the adsorption of MO onto B, B-CTAB, and BCTAB-Fe

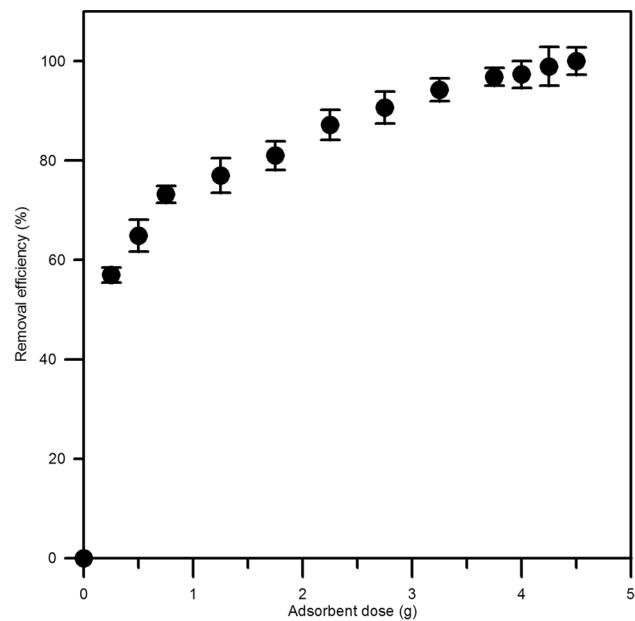


Fig. 8 Effect of adsorbent dose on the adsorption of MO onto B-CTAB-Fe

adsorption equilibrium constant.  $q_m$  (mg/g) is the maximum amount of adsorption in the monolayer formation state, and  $ce$  (mg/L) is the equilibrium concentration of the dye.  $k_f$  and  $n$  are Freundlich adsorption constants. The other parameters of Eq. 4 are the same as Eq. 3. The Freundlich equation is used for heterogeneous systems, irreversible adsorption, and non-monolayer adsorption. In comparison, the Langmuir adsorption isotherm is suitable for homogeneous surface and monolayer adsorption (Nataša et al. 2008). The basic properties of the Langmuir equation can be expressed by a dimensionless constant called the Langmuir  $R_L$  equilibrium parameter (Eq. 5).

$$R_L = \frac{1}{1 + k_L C_0} \tag{5}$$

where  $C_0$  (mg/L) is the initial concentration of the adsorbent and  $K_L$  (L/mg) is the Langmuir constant. The results of the sample absorption model are shown in Table 3. According to the data, the Langmuir isotherm diagram has a better regression coefficient than the Freundlich isotherm. Therefore, the Langmuir adsorption model is better suited to describe the adsorption of MO on the adsorbent. The results show that the surface of the synthesized adsorbents is homogeneous, and the available sites are uniformly present on the adsorbent surface. Given the value of  $R_L$  between zero and one, it can be concluded that the adsorption process is optimal for all three adsorbents. According to the results, the addition of CTAB has improved  $q_{max}$  and  $k_1$ . Although the addition of iron slightly reduces  $q_{max}$  and  $k_1$ , it adds regenerative properties to the adsorbent.

Since the adsorption kinetics of industrial effluent is an essential parameter in evaluating the effect of adsorbent, two kinetic models, pseudo-first-order and pseudo-second-order, were used to examine the data. The pseudo-first-order adsorption kinetics model has already been used for the adsorption of solid/liquid systems (Zaghouane-Boudiaf et al. 2014). These models are Eq. 6 and 7.

$$\log (q_e - q_t) = \log (q_e) - \frac{k_1}{2.303} t \tag{6}$$

$$\frac{t}{q_t} = \frac{1}{k_2 q_e^2} + \frac{1}{q_e} t \tag{7}$$

where  $k_1$  ( $\text{min}^{-1}$ ) is the adsorption rate constant,  $q_e$  and  $q_t$  (mg/g) are the adsorbent adsorption capacity at equilibrium time,  $t$  (s) time and  $k_2$  ( $\text{g} \cdot \text{mg}^{-1} \cdot \text{min}^{-1}$ ) are the adsorption rate constant. Figure 9 shows the agreement of the experimental data with the kinetic models. These results are summarized in Table 4. The correlation coefficient for all three adsorbents is higher in the pseudo-second-order equation. Also, the values of  $q$  obtained from the pseudo-second-order equation for all three types of adsorbents are more consistent with the values obtained with  $q_{exp}$ .

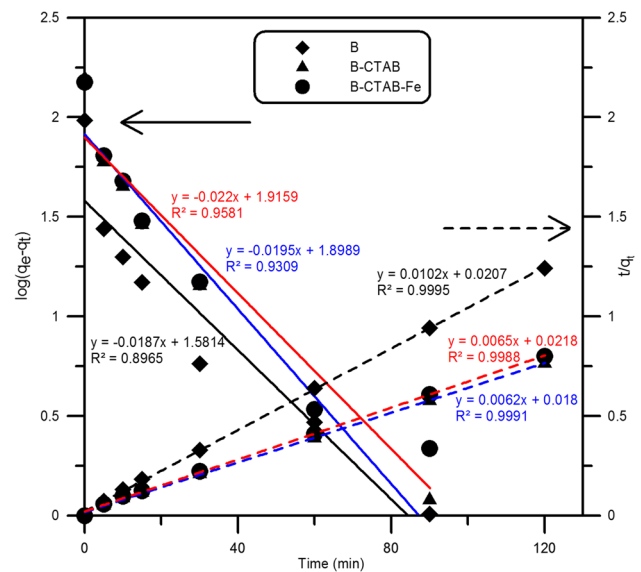


Fig. 9 The pseudo-first & second-order kinetics for the adsorption of MFO onto B, BCTAB, and B-CTAB-Fe

Table 3 Isotherm parameter analysis coefficient for the adsorption of MO onto B, B-CTAB, and B-CTAB-Fe

Isotherm constants	B	B-CTAB	B-CTAB-Fe
<b>Langmuir</b>			
$q_m$ (mg/g)	181.8181	212.7659	208.3333
$K_L$ (L/mg)	0.0114	0.0570	0.0402
$R^2$	0.9895	0.9906	0.9744
$R_L$	0.3048	0.0806	0.1106
<b>Freundlich</b>			
$K_f$ ( $\text{mg}^{1-(1/n)} \cdot \text{g}^{-1} \cdot \text{L}^{1/n}$ )	6.4387	31.4195	21.8172
$n$	1.7056	2.4943	2.1431
$R^2$	0.9443	0.8885	0.9044

Table 4 Kinetic models parameters obtained in adsorption of MO onto B, B-CTAB, and B-CTAB-Fe

Dynamics constants	B	B-CTAB	B-CTAB-Fe
<b>Pseudo-first-order</b>			
$q_e$ (mg/g)	38.1416	82.3948	79.2318
$k_1$ ( $\text{min}^{-1}$ )	0.0430	0.0506	0.0449
$R^2$	0.8965	0.9581	0.9309
<b>Pseudo-second-order</b>			
$q_e$ (mg/g)	98.0392	161.2903	153.8461
$k_2$ ( $\text{g} \cdot \text{mg}^{-1} \cdot \text{min}^{-1}$ )	0.0052	0.0021	0.0019
$R^2$	0.9995	0.9991	0.9988

**Table 5** Thermodynamic parameters for the adsorption of MO by B-CTAB-Fe

T(K)	$K_c$	$\Delta G^\circ$ (KJ/mol)	$\Delta H^\circ$ (KJ/mol)	$\Delta S^\circ$ (J/mol K)
303	6.94	-4.78	13.37	60.23
313	8.28	-5.48		
323	11.12	-6.08		

The thermodynamics of the adsorption process were studied using Eqs. 8 to 11.

$$G^\circ = -RT \ln K_C \quad (8)$$

$$\Delta G^\circ = \Delta H^\circ - T\Delta S^\circ \quad (9)$$

$$K_C = \frac{C_{Ae}}{C_e} \quad (10)$$

$$\ln K_C = + \frac{\Delta S^\circ}{R} - \frac{\Delta H^\circ}{RT} \quad (11)$$

$K_c$  is the ratio of the equilibrium concentration of the adsorbent surface  $c_{Ae}$  (mg/g) to the equilibrium concentration of the effluent in the solution  $c_e$  (mg/g).  $T$  (K) is the absolute temperature, and  $R$  (J/mol K) is the gas constant. The data in Table 5 are obtained by considering pH = 7, time 60 min, the concentration of dye solution 150 ppm, and amount of nano-adsorbent 0.75 g/l at three different temperatures. According to the results, enthalpy and entropy are positive, so the adsorption of methyl orange by the modified nano-adsorbent is an endothermic process, and with increasing temperature, the amount of colored effluent adsorption on the nano-adsorbent surface increases. A positive entropy value indicates that the randomness of the interface between the nano-adsorbent and the methyl orange dye solution increased during the adsorption process, indicating that structural changes occurred between the active nano-adsorbent sites the methyl orange dye solution (Uslu and Tanyol 2006; Abbasa and Trari 2015). According to Table 5, the negative amount of Gibbs free energy shows the spontaneity of the adsorption process for the synthesized nano-adsorbent (Eser et al. 2012).

Re-recycling of B-CTAB-Fe nano-adsorbent was performed by photo-Fenton. The adsorbed organic compounds on the adsorbent were bonded to the produced hydroxyl radicals and converted to  $\text{CO}_2$ ,  $\text{H}_2\text{O}$ ,  $\text{SO}_4^{2-}$  and  $\text{NO}_3^-$  then separated from the adsorbent surface, resulting in a white nano-adsorbent free of organic compounds. The percentage of dye removal efficiency by B-CTAB-Fe nano-adsorbent was 72.61% in the first recycling, 71.48% in the second time, and 69.50% in the third time. Yield percentages

after three times recycling indicate that the nano-adsorbent is well recycled in the photo-Fenton process.

## Conclusion

Under optimal conditions (pH = 7, time 60 min, concentration of dye solution 150 ppm, and amount of nano-adsorbent 0.75 g/l), maximum adsorption capacity and removal percentage were obtained. The percentage of MO removal by bentonite, B-CTAB, and B-CTAB-Fe is 46.8%, 76.88%, and 73.18%, respectively. Data from the photo-Fenton method for regenerating synthesized B-CTAB-Fe nano-adsorbent showed that solid-state ion-exchange bentonite with iron could be used as an effective nano-adsorbent.

**Author contribution** N.H., M.G., and M.S. contributed to the design and implementation of the research, to the analysis of the results, and to the writing of the manuscript. All authors read and approved the final manuscript.

**Availability of data and materials** Not applicable.

## Declarations

**Ethics approval** Not applicable.

**Consent to participate** Not applicable.

**Consent to publish** Not applicable.

**Competing interests** The authors declare no competing interests.

## References

- Abbasa M, Trari M (2015) Kinetic, equilibrium and thermodynamic study on the removal of Congo Red from aqueous solutions by adsorption onto apricot stone. *Proc Saf Environ Protect* 98:424–436
- Agarwal RM, Singh K (2017) Heavy metal removal from wastewater using various adsorbents: A review. *J Water Reuse Desalin* 7:387–419
- Ahmad A, Mohd-Setapar SH, Chuong CS, Khatoon A, Wani WA, Kumar R, Rafatullah M (2015) Recent advances in new generation dye removal technologies: novel search for approaches to reprocess wastewater. *RSC Adv* 5(39):30801–30818
- Ahmaruzzaman M (2008) Adsorption of phenolic compounds on low-cost adsorbents: a review. *Adv Colloid Interface Sci* 143:48–67
- Al-Asheh S, Banat F, Abu-Aitah L (2003) Adsorption of phenol using different types of activated bentonites. *Sep Purif Technol* 33(1):1–10
- Alexandre B, Langevin D, Médéric P, Aubry T, Couderc H, Nguyen Q, Saiter A, Marais S (2009) Water barrier properties of polyamide 12/montmorillonite nanocomposite membranes: structure and volume fraction effects. *J Membr Sci* 328(1–2):186–204



- Babuponnusami A, Muthukumar K (2014) A review on Fenton and improvements to the Fenton process for wastewater treatment. *J Environ Chem Eng* 2(1):557–572
- Ballav N, Das R, Giri S, Muliwa AM, Pillay K, Maity A (2018) L-Cysteine doped polypyrrole (Ppy@L-Cyst): A super adsorbent for the rapid removal of Hg +2 and efficient catalytic activity of the spent adsorbent for reuse. *Chem Eng J* 345:621–630
- Bouabidi ZB, El-Naas MH, Cortes D, McKay G (2018) Steel making dust as a potential adsorbent for the removal of lead (II) from an aqueous solution. *Chem Eng J* 334:837–844
- Bounab L, Draoui K, Ahrouch M, Hadri M, Bouchta D, Barhoun A (2017) An effective functionalized Moroccan bentonite: application for a green remediation of m-Cresol. *J Mater Environ Sci* 8(1):244–256
- Chacko JT, Subramaniam K (2011) Enzymatic degradation of azo dyes – a review. *Int J Environ Sci* 1(6):1250–1260
- Chen JP, Hausladen MC, Yang RT (1995) Delaminated Fe<sub>2</sub>O<sub>3</sub>-pillared clay: its preparation, characterization, and activities for selective catalytic reduction of NO by NH<sub>3</sub>. *J Catal* 151:135–146
- Chen Sh, Wu Y, Li G, Wu J, Meng G, Guo X, Liu Zh (2017) A novel strategy for preparation of an effective and stable heterogeneous photo-Fenton catalyst for the degradation of dye. *Appl Clay Sci* 136:103–111
- Darvishi Z, Morsali A (2011) Synthesis and characterization of nanobentonite by solvothermal method. *Colloids Surf A Physicochem Eng Aspects* 377(1–3):15–19
- De León MA, Rodríguez M, Marchetti SG, Sapag K, Faccio R, Sergio M, Bussi J (2017) Raw montmorillonite modified with iron for photo-Fenton processes: influence of iron content on textural, structural and catalytic properties. *J Environ Chem Eng* 5(5):4742–4750
- Deniz F, Karaman S (2011) Removal of basic red 46 dye from aqueous solution by pine treeleaves. *Chem Eng J* 170:67–74
- Dos Santos A, Viante MF, Pochapski DJ, Downs AJ, Almeida CAP (2018) Enhanced removal of p-nitrophenol from aqueous media by montmorillonite clay modified with a cationic surfactant. *J Hazard Mater* 355:136–144
- Douliad D, Leodopoloud Ch, Gimouhopoulos K, Rigas F (2009) Adsorption of humic acid on acid-activated Greek bentonite. *J Colloid Interface Sci* 340:131–141
- Eser A, Tirtom VN, Aydemir T, Becerik S, Dinçer A (2012) Removal of nickel (II) ions by histidine modified chitosan beads. *Chem Eng J* 210:590–596
- Fosso-Kankeu E, De Klerk CM, Van Aarde C, Waanders F, Phoku J, Pandey S (2016) Antibacterial activity of a synthesized chitosan-silver composite with different molecular weights chitosan against gram-positive and gram-negative bacteria. *Int'l Conf. on Advances in Science, Engineering, Technology & Natural Resources (ICA-SETNR-16)*, 142–146
- Ghaedi M, Mosallanejad N (2014) Study of competitive adsorption of malachite green and sunset yellow dyes on cadmium hydroxide nanowires loaded on activated carbon. *J Ind Eng Chem* 20(3):1085–1096
- Gong JM, Liu T, Wang XQ, Hu XL, Zhang LZ (2011) Efficient removal of heavy metal ions from aqueous systems with the assembly of anisotropic layered double hydroxide nanocrystals carbon nanosphere. *Environ Sci Technol* 45:6181–6187
- Gourouza M, Natatou I, Boos A (2011) Physico-chemical characterization of Sabon-Karré's Clay. *J Mater Environ Sci* 2(4):415–422
- Hadjltaief HB, Costa PD, Beaunier P, Gálvez ME, Zina MB (2014) Fe-clay-plate as a heterogeneous catalyst in photo-Fenton oxidation of phenol as probe molecule for water treatment. *Appl Clay Sci* 91–92:46–54
- Huang Z, Li Y, Chen W, Shi J, Zhang N, Wang X, Li Z, Gao L, Zhang Y (2017) Modified bentonite adsorption of organic pollutants of dye wastewater. *Mater Chem Phys* 202:266–276
- Hussin F, Aroua MK, Duad WMAW (2011) Textural characteristics, surface chemistry and activation of bleaching earth: a review. *Chem Eng J* 170(1):90–106
- Khatamian M, Divband B, Shahi R (2019) Ultrasound assisted coprecipitation synthesis of Fe<sub>3</sub>O<sub>4</sub>/ bentonite nanocomposite: performance for nitrate, BOD and COD water treatment. *J Water Process Eng* (31)
- Khelifi S, Ayari F (2019) Modified bentonite for anionic dye removal from aqueous solutions. Adsorbent regeneration by the photo-Fenton process. *C R Chim* 22:154–160
- Lellis B, Fávoro-Polonio CZ, Pamphile JA, Polonio JC (2019) Effects of textile dyes on health and the environment and bioremediation potential of living organisms. *Biotechnol Res Innov* 3(2):275–290
- Li YM, Bi ML, Wang ZP, Li R, Shi KL, Wu WS (2016) Organic modification of bentonite and its application for perchlorate (an analogue of pertechnetate) removal from aqueous solution. *J Taiwan Inst Chem Eng* 62:104–111
- Liu JF, Zhao ZS, Jiang GB (2008) Coating Fe<sub>3</sub>O<sub>4</sub> magnetic nanoparticles with humic acid for high efficient removal of heavy metal in water. *Environ Sci Technol* 42:6949–6954
- Ma X, Xu F, Chen L, Zhang Z (2005) Magnetic fluids for synthesis of the stable adduct  $\gamma$ -Fe<sub>2</sub>O<sub>3</sub>/CTAB/Clay. *J Cryst Growth* 280(1–2):118–125
- Mojsov KD, Andronikov D, Janevski A, Kuzelov A, Gaber S (2016) The application of enzymes for the removal of dyes from textile effluents. *Adv Technol* 5(1):81–86
- Moslemizadeh A, Khezerloo-ye Aghdam S, Shahbazi K, Khezerloo-ye Aghdam H, Alboghobeish F (2016) Assessment of swelling inhibitive effect of CTAB adsorption on montmorillonite in aqueous phase. *Appl Clay Sci* 127–128:111–122
- Nataša JJ, Nikolic AM, Gržetic I, Jovanovic D (2008) Organobentonite as efficient textile dye sorbent. *Chem Eng Technol* 31:567–574
- Nguyen TA, Juang RS (2013) Treatment of waters and wastewaters containing sulfur dyes: A review. *Chem Eng J* 219:109–117
- Rafatullah M, Sulaiman O, Hashim R, Ahmad A (2010) Adsorption of methylene blue on low-cost Adsorbents: a review. *J Hazard Mater* 177(1–3):70–80
- Schampera B, Šolc R, Tunega D, Dultz S (2016) Experimental and molecular dynamics study on anion diffusion in organically modified bentonite. *Appl Clay Sci* 120:91–100
- Simelane LP, Fosso-Kankeu E, Waanders F, Njobeh P, Pandey S (2016) Physico-Chemical treatment influenced by bacterial membrane and impact on dye adsorption capacity. In *Int'l Conf on Advances in Science, Engineering, Technology & Natural Resources (ICA-SETNR-16)*, pp 94–97. Parys (South Africa)
- Singh V, Singh SK, Pandey S, Sanghi R (2011) Synthesis and characterization of guar gum templated hybrid nano silica. *Int J Biol Macromol* 49(2):233–240
- Tang L, Yu J, Pang Y, Zeng G, Deng Y, Wang J, Ren X, Ye S, Peng B, Feng H (2018) Sustainable efficient adsorbent: Alkali-Acid modified magnetic biochar derived from sewage sludge for aqueous organic contaminant removal. *Chem Eng J* 336:160–169
- Tyagi, Chudasama CD, Jasra RV (2006) Determination of structural modification in acid activated montmorillonite clay by FT-IR spectroscopy. *Spectrochim Acta A Mol Biomol Spectrosc* 64(2):273–278
- Uslu G, Tanyol M (2006) Equilibrium and thermodynamic parameters of single and binary mixture biosorption of lead (II) and copper (II) ions onto *Pseudomonas putida*: effect of temperature. *J Hazard Mater* 135(1–3):87–93
- Yagub MT, Sen TK, Afroze S, Ang HM (2014) Dye and its removal from aqueous solution by adsorption: a review. *Adv Colloid Interface Sci* 209:172–184
- Yan H, Chen X, Feng Y, Xiang F, Li J, Shi Z, Wang X, Lin Q (2016) Modification of montmorillonite by ball-milling method for

- immobilization and delivery of acetamiprid based on alginate/exfoliated montmorillonite nanocomposite. *Polym Bull* 73:1185–1206
- Yu L, Luo YM (2014) The adsorption mechanism of anionic and cationic dyes by Jerusalem artichoke stalkbased mesoporous activated carbon. *J Environ Chem Eng* 2(1):220–229
- Yuan P, Yin X, He H, Yang D, Wang L, Zhu J (2006) Investigation on the delaminated-pillared structure of TiO<sub>2</sub>-PILC synthesized by TiCl<sub>4</sub> hydrolysis method. *Microporous Mesoporous Mater* 93(1–3):240–247
- Zaghouane-Boudiaf H, Boutahala M, Sahnoun S, Tiar C, Gomri F (2014) Adsorption characteristics, isotherm, kinetics, and diffusion of modified natural bentonite for removing the 2,4,5-trichlorophenol. *Appl Clay Sci* 90:81–87
- Zayed AM, Wahed MSA, Mohamed EA, Sillanpää M (2018) Insights on the role of organic matters of some Egyptian clays in methyl orange adsorption: isotherm and kinetic studies. *Appl Clay Sci* 166:49–60
- Zhang Z, Liao L, Xia Z (2010) Ultrasound-assisted preparation and characterization of anionic surfactant modified montmorillonites. *Appl Clay Sci* 50(4):576–581

**Publisher's note** Springer Nature remains neutral with regard to jurisdictional claims in published maps and institutional affiliations.